

LETTER TO THE EDITOR

Detection of the Schwarzschild precession in the orbit of the star S2 near the Galactic centre massive black hole

GRAVITY Collaboration*: R. Abuter⁸, A. Amorim^{6,13}, M. Bauböck¹, J.P. Berger^{5,8}, H. Bonnet⁸, W. Brandner³, V. Cardoso^{13,15}, Y. Clénet², P.T. de Zeeuw^{11,1}, J. Dexter^{14,1}, A. Eckart^{4,10}, F. Eisenhauer¹, N.M. Förster Schreiber¹, P. Garcia^{7,13}, F. Gao¹, E. Gendron², R. Genzel^{1,12}, S. Gillessen¹, M. Habibi¹, X. Haubois⁹, T. Henning³, S. Hippler³, M. Horrobin⁴, A. Jiménez-Rosales¹, L. Jochum⁹, L. Jocou⁵, A. Kaufer⁹, P. Kervella², S. Lacour², V. Lapeyrère², J.-B. Le Bouquin⁵, P. Léna², M. Nowak^{17,2}, T. Ott¹, T. Paumard², K. Perraut⁵, G. Perrin², O. Pfuhl^{8,1}, G. Rodríguez-Coira², J. Shangguan¹, S. Scheithauer³, J. Stadler¹, O. Straub¹, C. Straubmeier⁴, E. Sturm¹, L.J. Tacconi¹, F. Vincent², S. von Fellenberg¹, I. Waisberg^{16,1}, F. Widmann¹, E. Wieprecht¹, E. Wieworrek¹, J. Woillez⁸, S. Yazici^{1,4}, and G. Zins⁹

(Affiliations can be found after the references)

Draft version April 16, 2020

ABSTRACT

The star S2 orbiting the compact radio source Sgr A* is a precision probe of the gravitational field around the closest massive black hole (candidate). Over the last 2.7 decades we have monitored the star's radial velocity and motion on the sky, mainly with the SINFONI and NACO adaptive optics (AO) instruments on the ESO VLT, and since 2017, with the four-telescope interferometric beam combiner instrument GRAVITY. In this paper we report the first detection of the General Relativity (GR) Schwarzschild Precession (SP) in S2's orbit. Owing to its highly elliptical orbit ($e = 0.88$), S2's SP is mainly a kink between the pre- and post-pericentre directions of motion $\approx \pm 1$ year around pericentre passage, relative to the corresponding Kepler orbit. The superb 2017-2019 astrometry of GRAVITY defines the pericentre passage and outgoing direction. The incoming direction is anchored by 118 NACO-AO measurements of S2's position in the infrared reference frame, with an additional 75 direct measurements of the S2-Sgr A* separation during bright states ('flares') of Sgr A*. Our 14-parameter model fits for the distance, central mass, the position and motion of the reference frame of the AO astrometry relative to the mass, the six parameters of the orbit, as well as a dimensionless parameter f_{SP} for the SP ($f_{\text{SP}} = 0$ for Newton and 1 for GR). From data up to the end of 2019 we robustly detect the SP of S2, $\delta\phi \approx 12'$ per orbital period. From posterior fitting and MCMC Bayesian analysis with different weighting schemes and bootstrapping we find $f_{\text{SP}} = 1.10 \pm 0.19$. The S2 data are fully consistent with GR. Any extended mass inside S2's orbit cannot exceed $\approx 0.1\%$ of the central mass. Any compact third mass inside the central arcsecond must be less than about $1000 M_{\odot}$.

Key words. black hole physics – Galaxy: nucleus – gravitation – relativistic processes

1. Introduction

1.1. Testing GR and the massive black hole paradigm

The theory of General Relativity (GR) continues to pass all experimental tests with flying colours (Einstein 1916; Will 2014). High-precision laboratory and Solar System experiments, and observations of solar-mass pulsars in binary systems (Kramer et al. 2006; Kramer 2016) have confirmed GR in the low-curvature regime. Gravitational waves from several stellar mass, black hole (sBH) candidate in-spirals with LIGO (Abbott et al. 2016) have tested the strong-curvature limit.

General Relativity predicts black holes, that is, space-time solutions with a non-spinning or spinning central singularity cloaked by a communication barrier, an event horizon (cf. Schwarzschild 1916; Kerr 1965). The LIGO measurements cur-

rently provide the best evidence that the compact in-spiralling binaries are indeed merging sBHs, but see Cardoso & Pani (2019).

Following the discovery of quasars (Schmidt 1963), evidence has been growing that most massive galaxies harbour a central compact mass, perhaps in the form of a massive black hole (MBH: $10^6 - 10^{10} M_{\odot}$, Lynden-Bell & Rees 1971; Kormendy & Ho 2013; McConnell & Ma 2013). Are these compact mass concentrations truly MBHs, as predicted by GR? Evidence in favour comes from relativistically broadened, redshifted iron $K\alpha$ line emission in nearby Seyfert galaxies (Tanaka et al. 1995; Fabian et al. 2000), from stellar or gas motions very close to them (e.g. Moran et al. 1999), and high resolution millimetre imaging (Event Horizon Telescope Collaboration et al. 2019).

The nearest MBH candidate is at the centre of the Milky Way ($R_0 \approx 8$ kpc, $M_{\bullet} \approx 4 \times 10^6 M_{\odot}$, Genzel et al. 2010; Ghez et al. 2008). It is coincident with a very compact and variable X-ray, infrared, and radio source, Sgr A*, which in turn is surrounded by a very dense cluster of orbiting young and old stars. Radio and infrared observations have provided detailed information on the distribution, kinematics, and physical properties of this nuclear star cluster and hot, warm, and cold interstellar gas interspersed in it (cf. Genzel et al. 2010; Morris et al. 2012; Falcke & Markoff 2013). Groups in Europe at the ESO NTT & VLT and in the USA

* GRAVITY is developed in a collaboration by the Max Planck Institute for extraterrestrial Physics, LESIA of Observatoire de Paris/Université PSL/CNRS/Sorbonne Université/Université de Paris and IPAG of Université Grenoble Alpes / CNRS, the Max Planck Institute for Astronomy, the University of Cologne, the CENTRA - Centro de Astrofísica e Gravitação, and the European Southern Observatory. Corresponding authors: R. Genzel (genzel@mpe.mpg.de), S. Gillessen (ste@mpe.mpg.de), A. Eckart (eckart@ph1.uni-koeln.de).

at the Keck telescopes have carried out high-resolution imaging and spectroscopy of the nuclear star cluster over the past two and a half decades. They determined increasingly precise motions for more than 10^4 stars, and orbits for ≈ 50 (Schödel et al. 2002; Ghez et al. 2003, 2008; Eisenhauer et al. 2005; Gillessen et al. 2009b; Schödel et al. 2009; Meyer et al. 2012; Boehle et al. 2016; Fritz et al. 2016; Gillessen et al. 2017). These orbits, in particular the highly eccentric orbit of the $m_K \approx 14$ star S2 (or ‘S02’ in the UCLA nomenclature), have demonstrated that the gravitational potential is dominated by a compact source of $4.25 \times 10^6 M_\odot$, concentrated within the pericentre distance of S2. S2 appears to be a slowly rotating, single, main-sequence B-star of age ≈ 6 Myr (Martins et al. 2008; Habibi et al. 2017; Gravity Collaboration et al. 2017; Chu et al. 2018).

The location of the radio source Sgr A* coincides with that of the mass centroid to much better than 1 mas (Plewa et al. 2015; Sakai et al. 2019). Millimetre Very Long Baseline Interferometry (Falcke et al. 2000; Doeleman et al. 2008; Johnson et al. 2017; Issaoun et al. 2019) shows that Sgr A* has a 1.3 mm half-light radius smaller than $18 \mu\text{as}$, or 1.8 times the Schwarzschild radius (R_S) of a $4.25 \times 10^6 M_\odot$ MBH. Sgr A* shows no detectable intrinsic motion within the international celestial reference frame ICRF. This supports the interpretation that the compact radio source is coincident with the mass (Reid & Brunthaler 2004; Reid et al. 2009; Reid & Brunthaler 2020). The Galactic Centre (GC) currently provides the best ‘laboratory’ for testing GR near MBHs and ultimately for testing the MBH paradigm (Alexander 2005, 2017; Genzel et al. 2010; Psaltis et al. 2016).

1.2. Detection of GR effects in the orbits of stars around Sgr A*: Gravitational redshift

Following the observations of the pericentre passage of S2 in 2002.33 (Schödel et al. 2002; Ghez et al. 2003) it became clear that the first-order ($O(\beta^2)$, $\beta = v/c$) GR-effects of the orbit may be in reach of precision observations. These are the gravitational redshift (RS) $\text{PPN1}_{\text{RS}}(\lambda)$, and the Schwarzschild precession (SP) $\text{PPN1}_{\text{SP}}(x, y)$, see Rubilar & Eckart (2001), Zucker et al. (2006), Angéilil et al. (2010), Angéilil & Saha (2014), Grould et al. (2017), and Parsa et al. (2017). For this purpose, a significant (factor 4–10) improvement in astrometry compared to what was possible in 2010 was needed. We achieved this goal with the development of GRAVITY, a cryogenic, interferometric beam combiner of all four UTs of the ESO VLT, along with adaptive optics (AO) systems for all four UTs, and a laser metrology system (Gravity Collaboration et al. 2017).

On May 19, 2018 (2018.38), S2 passed pericentre at 120 AU ($\approx 1400 R_S$) with an orbital speed of 7700 km/s ($\beta = 0.026$). From monitoring the star’s radial velocity and motion on the sky from data taken prior to and up to two months after pericentre, Gravity Collaboration et al. (2018a) were able to detect the first post-Newtonian effect of GR, the gravitational redshift, along with the transverse Doppler effect of special relativity (SRT, Misner et al. 1973). Gravity Collaboration et al. (2019) improved the statistical robustness of the detection of the RS to $f_{\text{RS}} = 1.04 \pm 0.05$, where the dimensionless parameter f_{RS} is 0 for Newtonian orbits and 1 for GR-orbits. Do et al. (2019) confirmed these findings from a second, independent data set mainly from the Keck telescope, $f_{\text{RS}} = 0.88 \pm 0.17$.

The combined $\text{PPN1}_{\text{RS}}(\lambda)$ gravitational redshift and transverse Doppler effect are detected as a 200 km/s residual centred on the pericentre time, relative to the $f_{\text{RS}} = 0$ orbit (with the same other parameters describing the star’s orbit and the gravitational potential). While the RS occurs solely in wavelength-space, the

superior astrometric capabilities of GRAVITY serve to set much tighter constraints on the orbital geometry, mass and distance, thus decreasing the uncertainty of f_{RS} more than three times relative to data sets constructed from single-telescope, AO imaging and spectroscopy.

In the following we report the first measurement of the next relativistic effect in the orbit of S2, namely the in-plane, prograde precession of its pericentre angle, the Schwarzschild precession (Misner et al. 1973).

2. Observations

Following on from Gravity Collaboration et al. (2018a, 2019), we expand in this paper our analysis of the positions and K-band spectra of the star S2 by another year, to fall of 2019. This yielded 5 additional NACO points, 6 SINFONI points and, especially, 11 crucial GRAVITY points. We now have

- 118 measurements with the VLT AO-assisted infrared camera NACO (Lenzen et al. 1998; Rousset et al. 1998) between 2002 and 2019.7 of the position of S2 in the K or H bands, relative to the ‘Galactic Centre infrared reference system’ (Plewa et al. 2015, rms uncertainty $\approx 400 \mu\text{as}$). This means that between the 2002.33 pericentre passage until 2019.7 we have 7 to 16 NACO positional measurements per year. Between 1992 and 2002, we also used the speckle camera SHARP at the NTT (Hofmann et al. 1993), but the astrometry of the speckle data on a 3.5 m telescope is an order of magnitude worse than the AO imagery on the 8 m VLT (rms uncertainty ≈ 3.8 mas);
- 75 NACO measurements between 2003.3 and 2019.7 of the direct S2-Sgr A* separation during bright states of Sgr A* (typical rms uncertainty 1.7 mas);
- 54 GRAVITY measurements between 2016.7 and 2019.7 of the S2-Sgr A* separation (rms uncertainty $\approx 65 \mu\text{as}$). During the pericentre-passage year 2018, the sampling was especially dense with 25 measurements;
- 92 spectroscopic measurements of the $2.167 \mu\text{m}$ HI (Br γ) and the $2.11 \mu\text{m}$ HeI lines between 2003.3 and 2019.45 with the AO-assisted integral field spectrometer SINFONI at the VLT (Eisenhauer et al. 2003; Bonnet et al. 2003), with an uncertainty of ≈ 12 km/s (Gravity Collaboration et al. 2019). This means that we typically have 3 to 6 spectroscopic measurements per year, and more than 20 in 2018. We also added 2 more NACO AO slit spectroscopic measurements from 2003, and 3 more Keck-NIRC2 AO spectroscopic measurements between 2000 and 2002 (Do et al. 2019).

The SHARP and NACO data deliver relative positions between stars in the nuclear star cluster, which are then registered in the radio frame of the GC (Reid et al. 2009; Reid & Brunthaler 2020) by multi-epoch observations of nine stars in common between the infrared and radio bands. Another important step is the correction for spatially variable image distortions in the NACO imager, which are obtained from observations of an HST-calibrated globular cluster (Plewa et al. 2015). The radio calibrations still allow for a zero-point offset and a drift of the radio-reference frame centred on Sgr A* (strictly speaking, on the mass-centroid) with respect to the infrared reference frame, which we solve for empirically in our orbit fitting. For this purpose, we use the Plewa et al. (2015) radio-to-infrared reference frame results as a prior ($x_0 = -0.2 \pm 0.2$ mas, $y_0 = 0.1 \pm 0.2$ mas, $v_{x_0} = 0.05 \pm 0.1$ mas/yr, $v_{y_0} = 0.06 \pm 0.1$ mas/yr). These reference frame parameters (x_0 , y_0 , v_{x_0} , and v_{y_0}) are now the limiting factor in the precision of the detection of the SP of S2.

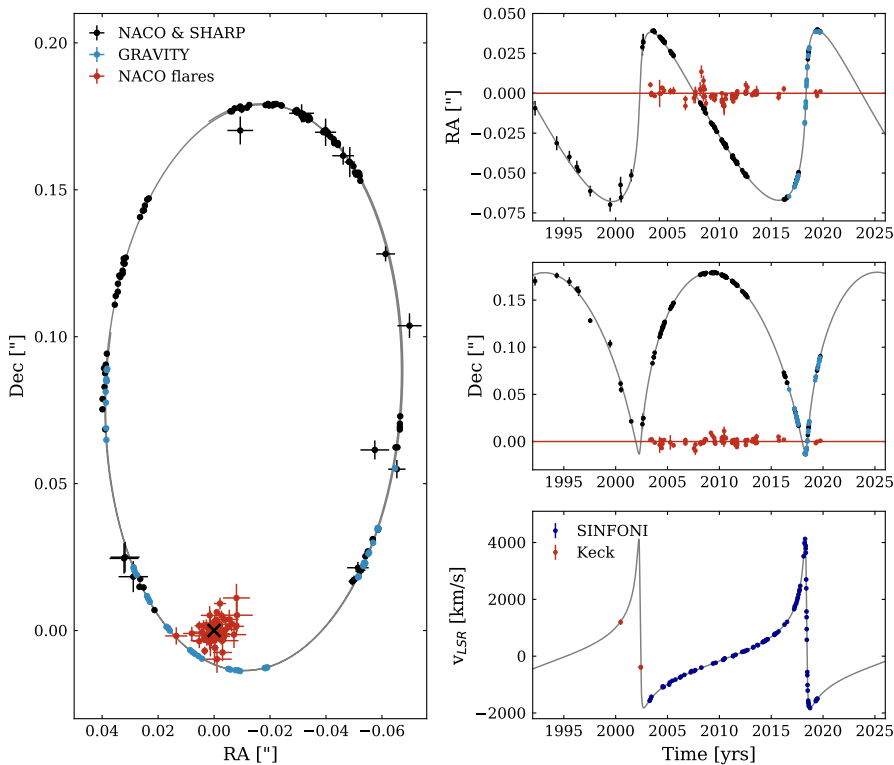


Fig. 1. Summary of the observational results of monitoring the S2-Sgr A* orbit from 1992 to the end of 2019. Left: SHARP, NACO (black points), and GRAVITY (blue points) astrometric positions of the star S2, along with the best-fitting GR orbit (grey line). The orbit does not close as a result of the SP. The mass centre is at (0,0), marked by the cross. All NACO and SHARP points were corrected for a zero-point offset and drift in RA and Dec. The red data points mark the positions of the infrared emission from Sgr A* during bright states, where the separation of S2 and Sgr A* can be directly inferred from differential imaging. Right: RA (top) and Dec (middle) offset of S2 (black and blue) and of the infrared emission from Sgr A* (red) relative to the position of Sgr A* (assumed to be identical with the mass centre). Grey is the best-fitting GR-orbit including the Rømer effect (finite speed of light), SRT, and GR to PPN1. We assumed $f_{RS} = 1$ and fitted for f_{SP} . Bottom right: Same for the line-of-sight velocity of the star.

The situation is different for GRAVITY. Here we detect and stabilise the interferometric fringes on the star IRS16C located $\approx 1''$ NE of Sgr A*, and observe S2 or Sgr A* within the second phase-referenced fibre (see Gravity Collaboration et al. 2017), such that the positional difference between S2 and Sgr A* can be determined to $< 100 \mu\text{as}$ levels (see Appendix A.1). To obtain this accuracy, the measurements of S2 and Sgr A* are made within a short time interval and linked together interferometrically (Appendix A.2). Between the end of 2017 and throughout 2018, S2 and Sgr A* are simultaneously detected in a single fibre-beam positioning as two unresolved sources in $> 95\%$ of our individual integrations (5 min each), such that the S2-Sgr A* distance is even more directly obtained in each of these measurements (Appendix A.3). The development over time of the astrometric and spectroscopic measurement uncertainties are summarised in Figure A.3. For more details on the data analysis of all three instruments we refer to Gravity Collaboration et al. (2017, 2018a,b, 2019) and Appendix A.

3. Results

3.1. Schwarzschild precession in the S2 orbit

Figure 1 shows the combined single-telescope and interferometric astrometry of the 1992-2019 sky-projected orbital motion of S2 and the line-of sight velocity of the star. The almost 100-fold improvement of statistical astrometric measurement precision in the past 27 years is one key for detecting the SP in the S2 orbit. As discussed in Section 2, the accurate definition of the reference frame for the NACO data is the second key. The robustness of the detection of the SP strongly correlates with the precision of knowing $(x_0, y_0, vx_0, and vy_0)$, as this sets the angle of the orbit at the last apocentre (2010.35). Using the priors from Plewa et al. (2015), we fitted these four reference frame parameters in our posterior fitting, but we found the additional constraints obtained from Sgr A*-S2 flare offsets in NACO to be very helpful.

To this end, we included in the calculation of χ^2 the constraint that the flare positions are tracing the mass centre.

Confusion of S2 with nearby other sources is the final key issue (see also Gillessen et al. 2009b, 2017; Plewa & Sari 2018; Do et al. 2019). Ghez et al. (2003) and Schödel et al. (2002) already have noted that the NACO or NIRC2 AO astrometry at times was unreliable and biased over longer periods of time (0.5–1.5 years). These systematic position excursions are mainly caused by confusion, that is, the positional pulling of the apparent sky position of S2 by a passing nearby background object. This issue is especially detrimental when the variable Sgr A* emission source is within the diffraction limit of the telescope (Ghez et al. 2003, 2008; Plewa & Sari 2018; Do et al. 2019), making the 2002 and 2018 AO astrometry more uncertain or even unusable. Fortunately, GRAVITY removed any need for AO imagery during the 2018 pericentre passage, therefore we excised most of the 2002 and 2018 NACO astrometry from our data set. We identified further confusion events with fainter stars passing close to S2 on a number of occasions (e.g. 1998, 2006, and 2013/2014) and removed these questionable data points.

At pericentre R_{peri} , S2 moves with a total space velocity of $\approx 7700 \text{ km/s}$, or $\beta = v/c = 2.56 \times 10^{-2}$. The SP of the orbit is a first-order (β^{2N} , $N = 1$) effect in the parametrised post-Newtonian (PPN, cf. Will & Nordvedt 1972) expansion, $\text{PPN}(1) \approx \beta^2 \approx R_S/R_{\text{peri}} \approx 6.6 \times 10^{-4}$. We used the post-Newtonian expansion of Will (2008) and added a factor f_{SP} in the equation of motion in front of the Schwarzschild-related terms (see Appendix C). This corresponds to (e.g. Misner et al. 1973)

$$\Delta\phi_{\text{per orbit}} = \text{PPN1}_{\text{SP}} = f_{\text{SP}} \frac{3\pi R_S}{a(1-e^2)} \stackrel{\text{for S2}}{=} f_{\text{SP}} \times 12.1' \quad (1)$$

Here a is the semi-major axis and e is the eccentricity of the orbit. The quantity f_{SP} can then be used as a fitting parameter, similar to our approach for the RS (Gravity Collaboration et al. 2018b, 2019). Appendix B explains the effects that the SP should have on the measured parameters of the S2 orbit.

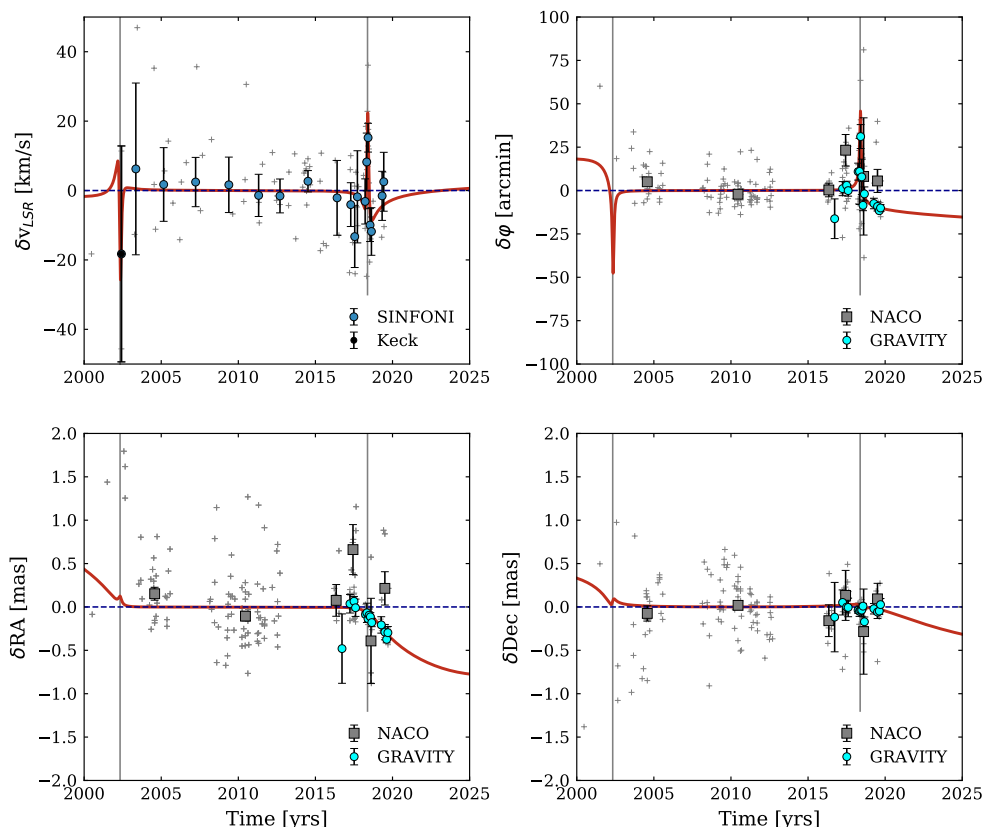


Fig. 2. Posterior analysis of all data by fitting for f_{SP} simultaneously with all other parameters. As in Figure B.2, the bottom panels show the residuals in RA (left) and Dec (right) between the data and the best-fitting GR (thick red curve, $f_{\text{SP}} = 1.1$), relative to the same orbit for $f_{\text{SP}} = 0$ (Newton, plus Rømer effect, plus SRT, plus RS). Grey crosses denote individual NACO or SINFONI data, cyan filled black circles show averaged GRAVITY data, and grey rectangles denote averages of the NACO data. The top right panel shows the same for $\delta\varphi$, and the top left panel for δv_z . Blue filled black circles are averages of the SINFONI residuals, with all residuals shown as grey crosses. The best fit (red curve) including the flare data (Figure 1) has $f_{\text{SP}} = 1.1$, with a 1σ uncertainty of 0.19. The overall reduced χ_r^2 of this fit is 1.5.

3.2. Posterior analysis

The six parameters describing the Kepler orbit (a , e , i , ω , Ω , and t_0), the distance, and the central mass, and the five coordinates describing the position on the sky and the three-dimensional velocity of the reference frame (relative to the AO spectroscopic or imaging frames) all have uncertainties. In particular, distance and mass are uncertain and correlated. Following Gravity Collaboration et al. (2018a, 2019), we determined the best-fit value of the parameter f_{SP} a posteriori, including all data and fitting for the optimum values of all parameters with the Levenberg-Marquardt χ^2 -minimisation algorithm (Levenberg 1944; Marquardt 1963), including prior constraints. It is essential to realise that the inferred measurement uncertainties are affected and partially dominated by systematic effects, especially when the evidence from three or more very different measurement techniques is combined.

Figures 2 and 3 show the fit results when we simultaneously fitted the data and the flare positions. As priors we used the Plewa et al. (2015) reference frame results (see Section 2). All data prior to the 2018.3 pericentre passage are fit by $f_{\text{SP}} \approx 0$ (Newton, plus Rømer effect, plus SRT, plus RS). The residuals in this period are consistent with 0 (bottom panels of Figure 2). The GRAVITY data between 2017 and 2019.7 clearly show that the post-pericentre orbit exhibits a sudden kink, mainly in RA. The data are compatible with a pure in-plane precession. This is shown in the upper right panels of Figures 2 and 3, where we have computed the residuals in the projected angle of the SP-fitted orbit on the sky $\delta\varphi(t)$, relative to the $f_{\text{SP}} = 0$ orbit. This is exactly as expected from an $f_{\text{SP}} \approx 1$ GR orbit (Figure B.2). The more subtle swings in δRA , δDec , δv_z , and $\delta\varphi$ predicted by GR (Figure B.2) are detected as well (see Appendix B for a more detailed discussion).

Table E.1 lists the best-fit parameters and their 1σ uncertainties. Depending on the weighting of different data sets and the choice of priors, we find that the best-fitting f_{SP} value varies between 0.9 and 1.2, with a fiducial value of $f_{\text{SP}} = 1.1$. The formal statistical fit uncertainty of this parameter does not depend much on the selection of astrometric and spectroscopic data of S2. The value of its rms uncertainty Δf_{SP} does depend on the methodology of error treatment. The distribution of the NACO flare position residuals shows significant non-Gaussian outliers. There are \approx six (of 75 data points) $> 4\sigma$ outliers above the rms of ≈ 1.7 mas. If the χ^2 distribution and the weighting of these points are treated as if they had a normal distribution, the reduced χ_r^2 of our overall fits is driven up to ≈ 1.65 , for a total χ^2 of 995. In this case $\Delta f_{\text{SP}} = 0.204$. These outliers can be down-weighted by replacing the penalty function $p(r) = r^2$ in the calculation of $\chi^2 = \sum p((\text{data} - \text{model})/\text{error})$ with $p(r, s) = r^2 \cdot s^2 / (r^2 + s^2)$, $s = 10$. This introduces a soft cut-off around 10σ in how much a data point can maximally contribute to the χ^2 . With this scheme, χ_r^2 of the overall fit drops to 1.50, and $\Delta f_{\text{SP}} = 0.194$.

We also fitted the data by solving simultaneously for f_{SP} and f_{RS} , without fixing the RS term to 1. In this case we find $f_{\text{SP}} = 0.99 \pm 0.24$ and $f_{\text{RS}} = 0.965 \pm 0.042$ (with the outlier damper on), again fully consistent with GR.

An alternative approach is to place the reference frame constraints we obtained from the flare positions into a combined prior with the constraints from Plewa et al. (2015). In this case the prior for the location of Sgr A* in the NACO infrared frame is $x_0 = -0.42 \pm 0.15$ mas, $y_0 = 0.30 \pm 0.15$ mas, $v_{x0} = -0.02 \pm 0.05$ mas/yr, and $v_{y0} = 0.015 \pm 0.05$ mas/yr. When we use this prior to fit only the S2 data, we obtain $f_{\text{SP}} = 0.92 \pm 0.22$ and $\chi_r^2 = 0.88$ ($\chi^2 = 398$).

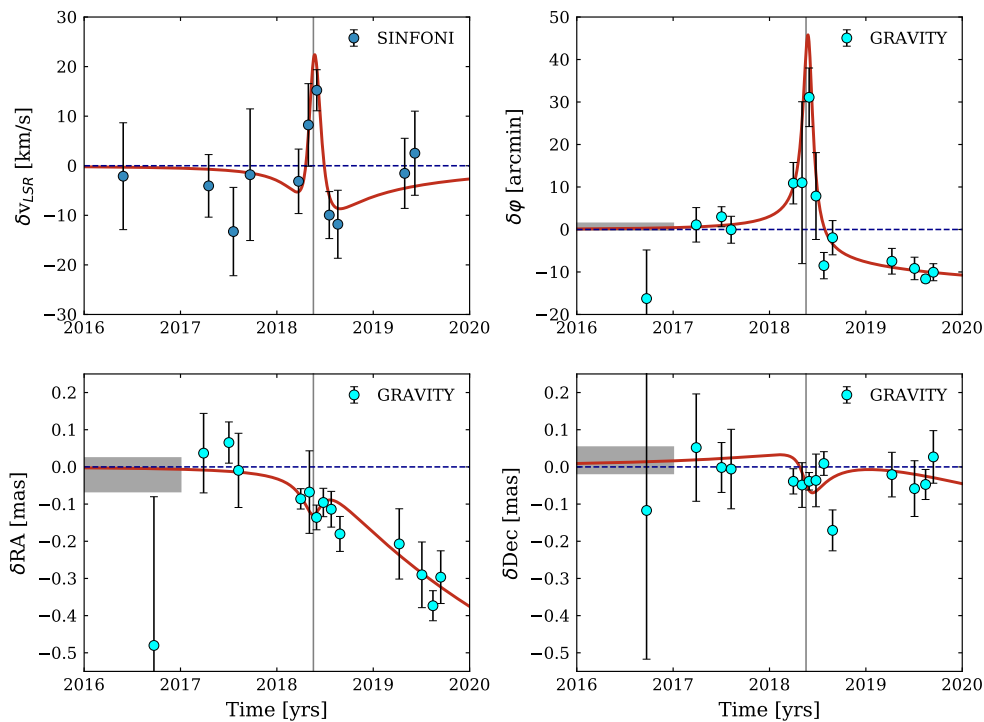


Fig. 3. As Figure 2, but now zooming into the critical 2018 pericentre residuals (best-fit $f_{\text{SP}} = 1.1$ minus $f_{\text{SP}} = 0$, with all other parameters fixed). In the bottom two and the top right panels, blue filled, open black circles (with 1σ uncertainties) are averages of GRAVITY data. The grey bar on the left denotes the constraints obtained from NACO imagery of S2 and Sgr A* flares on the location of the apocentre value (2010.35). Averages (and 1σ uncertainties) of the radial velocity residuals from SINFONI are open black, blue filled circles (top left). The residuals of the best-fitting $f_{\text{SP}} = 1.1$ minus $f_{\text{SP}} = 0$ curves are plotted in red.

Fitting the orbit with $f_{\text{SP}} = 0$ fixed yields $\chi^2 = 932.3$, compared to 906.4 with $f_{\text{SP}} = 1$ fixed. The corresponding difference in Bayesian information criterion (Claesekens & Hjort 2008) $\Delta\text{BIC} = 25.9$ yields very strong evidence that the GR model describes the data better than the best-fitting Kepler (with SRT, RS, and Rømer delay included) orbit.

Gravity Collaboration et al. (2018b) showed that the near-infrared emission of Sgr A* during bright flares exhibits clockwise loop motions of excursions $50 - 100 \mu\text{as}$. The typical flare duration and the orbital timescale are ≈ 1 hour. A stationary offset between the infrared emission and the mass centroid of that size would induce a change of up to ± 0.2 in f_{SP} , comparable to the overall uncertainty in f_{SP} . During a typical time of several hours making up a GRAVITY data point in this work these fluctuations should average out to less than $10 \mu\text{as}$ such that the additional error on f_{SP} is well below the statistical error.

Next we carried out a Markov-Chain Monte Carlo (MCMC) analysis. Using 200,000 realisations we found that the distribution of f_{SP} is well described by a Gaussian centred on $f_{\text{SP}} = 1.11 \pm 0.21$ (Figure E.1, and see Appendix E for more details). The largest relative uncertainty in the determination of the Schwarzschild term originates in the degeneracy of f_{SP} with the pericentre time (see Appendix B) and with the zero-point x_0 of the long-term reference frame (mass vs. NACO imaging coordinates). This is expected because the precession is largest in the EW direction.

Furthermore, we compared our first-order post-Newtonian code with fully relativistic GR orbits using the GYOTO ray-tracing code¹ (Vincent et al. 2011; Grould et al. 2017). As expected, the deviations are small. The largest differences over the full data range are $\Delta\text{RA} = 62 \mu\text{as}$, $\Delta\text{Dec} = 41 \mu\text{as}$ and $\Delta v_z = 11.4 \text{ km/s}$, occurring for a short time around pericentre. Moreover, the Bayesian comparison between the best-fitting full-GR and Kepler (with SRT, RS, and Rømer delay included) orbits strongly prefers the GR model.

Finally, we also included the data from Do et al. (2019) (excepting the 2018 astrometry) using the scheme in Gillessen et al. (2009a) allowing for an additional offset in position and velocity for the Keck reference system. The 18-parameter fit yields a consistent result, but no further improvement.

4. Conclusions

We have presented the first direct detection of the in-plane Schwarzschild precession around Sgr A* in the GC. Our results are fully consistent with GR. We detect the precession of S2 robustly at the 5 to 6σ level in posterior fitting and MCMC analysis. Our result is independent of the fit methodology, data selection, weighting, and error assignments of individual data points. The significance of our result depends mostly on how accurately we can constrain $(x_0, y_0, vx_0, \text{ and } vy_0)$. The success rests crucially on the superior GRAVITY astrometry during and past pericentre passage on the one hand, and on 75 measurements of Sgr A* flares from NACO AO data between 2003 and 2019 on the other. The flare data allow us to independently constrain the zero-point of the NACO reference frame.

Additional masses in the GC would lead to Newtonian perturbations of the S2 orbit. An extended mass component (e.g. composed of stars or remnants, but also of other particles) would result in a retrograde precession. The presence of a second massive object would lead to short excursions in the smooth orbit figure. Our data place tight constraints on both, which we detail in Appendix D, where we discuss several important astrophysical implications of our measurements.

We expect only modest further improvement of the significance of our result as our monitoring continues and S2 moves away from pericentre, because our result already now is limited by the precision with which we have measured the pre-pericentre orbit with AO data.

¹ Freely available at <http://gyoto.obspm.fr>

Acknowledgements. We are very grateful to our funding agencies (MPG, ERC, CNRS [PNCG, INGRAM], DFG, BMBF, Paris Observatory [CS, PhyFOG], Observatoire des Sciences de l'Univers de Grenoble, and the Fundação para a Ciência e Tecnologia), to ESO and the ESO/Paranal staff, and to the many scientific and technical staff members in our institutions, who helped to make NACO, SINFONI, and GRAVITY a reality. S.G. acknowledges the support from ERC starting grant No. 306311. F.E. and O.P. acknowledge the support from ERC synergy grant No. 610058. A.A., P.G. and, V.G. were supported by Fundação para a Ciência e a Tecnologia, with grants reference UIDB/00099/2020 and SFRH/BSAB/142940/2018.

References

- Abbott, B. P., Abbott, R., Abbott, T. D., et al. 2016, *Physical Review Letters*, 116, 061102
- Alexander, T. 2005, *Physics Reports*, 419, 65
- Alexander, T. 2017, *ARA&A*, 55, 17
- Angélic, R. & Saha, P. 2014, *MNRAS*, 444, 3780
- Angélic, R., Saha, P., & Merritt, D. 2010, *ApJ*, 720, 1303
- Bartko, H., Martins, F., Fritz, T. K., et al. 2009, *ApJ*, 697, 1741
- Baumgardt, H., Amaro-Seoane, P., & Schödel, R. 2018, *A&A*, 609, A28
- Boehle, A., Ghez, A. M., Schödel, R., et al. 2016, *ApJ*, 830, 17
- Bonnet, H., Ströbele, S., Biancat-Marchet, F., et al. 2003, *Proc. SPIE Vol.*, 4839, 329
- Cardoso, V. & Pani, P. 2019, *Living Reviews in Relativity*, 22, 4
- Chu, D. S., Do, T., Hees, A., et al. 2018, *ApJ*, 854, 12
- Claesekens, G. & Hjort, N. L. 2008, *Model Selection and Model Averaging* (Cambridge University Press)
- Do, T., Hees, A., Ghez, A., et al. 2019, *Science*, 365, 664
- Doeleman, S. S., Weintroub, J., Rogers, A. E. E., et al. 2008, *Nature*, 455, 78
- Einstein, A. 1916, *Annalen der Physik*, 354, 769
- Eisenhauer, F., Abuter, R., Bickert, K., et al. 2003, in *Proc. SPIE*, Vol. 4841, Instrument Design and Performance for Optical/Infrared Ground-based Telescopes, ed. M. Iye & A. F. M. Moorwood, 1548–1561
- Eisenhauer, F., Genzel, R., Alexander, T., et al. 2005, *ApJ*, 628, 246
- Event Horizon Telescope Collaboration, Akiyama, K., Alberdi, A., et al. 2019, *ApJ*, 875, L1
- Fabian, A. C., Iwasawa, K., Reynolds, C. S., & Young, A. J. 2000, *PASP*, 112, 1145
- Falcke, H. & Markoff, S. B. 2013, *Classical and Quantum Gravity*, 30, 244003
- Falcke, H., Melia, F., & Agol, E. 2000, *ApJ*, 528, L13
- Fritz, T. K., Chatzopoulos, S., Gerhard, O., et al. 2016, *ApJ*, 821, 44
- Gainutdinov, R. I. 2020, arXiv e-prints, arXiv:2002.12598
- Genzel, R., Eisenhauer, F., & Gillessen, S. 2010, *Rev. Mod. Phys.*, 82, 3121
- Ghez, A., Duchêne, G., Matthews, K., et al. 2003, *ApJ Letters*, 586, 127
- Ghez, A., Salim, S., Weinberg, N. N., et al. 2008, *ApJ*, 689, 1044
- Gillessen, S., Eisenhauer, F., Fritz, T. K., et al. 2009a, *ApJ*, 707, L114
- Gillessen, S., Eisenhauer, F., Trippe, S., et al. 2009b, *ApJ*, 692, 1075
- Gillessen, S., Plewa, P. M., Eisenhauer, F., et al. 2017, *ApJ*, 837, 30
- Gondolo, P. & Silk, J. 1999, *Phys. Rev. Lett.*, 83, 1719
- Gravity Collaboration, Abuter, R., Accardo, M., et al. 2017, *A&A*, 602, A94
- Gravity Collaboration, Abuter, R., Amorim, A., et al. 2018a, *A&A*, 615, L15
- Gravity Collaboration, Abuter, R., Amorim, A., et al. 2019, *A&A*, 625, L10
- Gravity Collaboration, Abuter, R., Amorim, A., et al. 2018b, *A&A*, 618, L10
- Gould, M., Vincent, F. H., Paumard, T., & Perrin, G. 2017, *A&A*, 608, A60
- Gualandris, A., Gillessen, S., & Merritt, D. 2010, *MNRAS*, 409, 1146
- Gualandris, A. & Merritt, D. 2009, *ApJ*, 705, 361
- Habibi, M., Gillessen, S., Martins, F., et al. 2017, *ApJ*, 847, 120
- Hansen, B. M. S. & Milosavljević, M. 2003, *ApJ*, 593, L77
- Hees, A., Do, T., Ghez, A. M., et al. 2017, *Physical Review Letters*, 118, 211101
- Hofmann, R., Eckart, A., Genzel, R., & Drapatz, S. 1993, *Ap&SS*, 205, 1
- Issaoun, S., Johnson, M. D., Blackburn, L., et al. 2019, *ApJ*, 871, 30
- Johnson, M. D., Bouman, K. L., Blackburn, L., et al. 2017, *ApJ*, 850, 172
- Kerr, R. P. 1965, in *Quasi-Stellar Sources and Gravitational Collapse*, ed. I. Robinson, A. Schild, & E. L. Schucking, 99
- Kormendy, J. & Ho, L. C. 2013, *ARA&A*, 51, 511
- Kramer, M. 2016, *International Journal of Modern Physics D*, 25, 1630029
- Kramer, M., Stairs, I. H., Manchester, R. N., et al. 2006, *Science*, 314, 97
- Lacroix, T. 2018, *A&A*, 619, A46
- Lenzen, R., Hofmann, R., Bizenberger, P., & Tuschke, A. 1998, *Proc. SPIE Vol.*, 3354, 606
- Levenberg, K. 1944, *Quart. Appl. Math.*, 2, 164
- Lynden-Bell, D. & Rees, M. J. 1971, *MNRAS*, 152, 461
- Marquardt, D. W. 1963, *J. Soc. Indust. Appl. Math.*, 11, 431
- Martins, F., Gillessen, S., Eisenhauer, F., et al. 2008, *ApJ Letters*, 672, 119
- McConnell, N. J. & Ma, C.-P. 2013, *ApJ*, 764, 184
- Merritt, D., Alexander, T., Mikkola, S., & Will, C. M. 2010, *Phys. Rev. D*, 81, 062002
- Merritt, D., Gualandris, A., & Mikkola, S. 2009, *ApJ*, 693, L35
- Meyer, L., Ghez, A., Schödel, R., et al. 2012, *Science*, 338, 84
- Misner, C. W., Thorne, K. S., & Wheeler, J. A. 1973, *Gravitation* (W.H. Freeman, Princeton Univers. Press)
- Moran, J. M., Greenhill, L. J., & Herrnstein, J. R. 1999, *Journal of Astrophysics and Astronomy*, 20, 165
- Morris, M. R., Meyer, L., & Ghez, A. M. 2012, *Research in Astronomy and Astrophysics*, 12, 995
- Mouawad, N., Eckart, A., Pfalzner, S., et al. 2005, *Astronomische Nachrichten*, 326, 83
- Naos, S., Will, C. M., Ramirez-Ruiz, E., et al. 2020, *ApJ*, 888, L8
- Navarro, J. F., Frenk, C. S., & White, S. D. M. 1996, *ApJ*, 462, 563
- Parsa, M., Eckart, A., Shahzamanian, B., et al. 2017, *ApJ*, 845, 22
- Paumard, T., Genzel, R., Martins, F., et al. 2006, *ApJ*, 643, 1011
- Perrin, G. & Woillez, J. 2019, *A&A*, 625, A48
- Plewa, P. M., Gillessen, S., Eisenhauer, F., et al. 2015, *MNRAS*, 453, 3234
- Plewa, P. M. & Sari, R. 2018, *MNRAS*, 476, 4372
- Plummer, H. C. 1911, *MNRAS*, 71, 460
- Psaltis, D. 2004, in *American Institute of Physics Conference Series*, Vol. 714, X-ray Timing 2003: Rossi and Beyond, ed. P. Kaaret, F. K. Lamb, & J. H. Swank, 29–35
- Psaltis, D., Wex, N., & Kramer, M. 2016, *ApJ*, 818, 121
- Reid, M. J. & Brunthaler, A. 2004, *ApJ*, 616, 872
- Reid, M. J. & Brunthaler, A. 2020, arXiv e-prints, arXiv:2001.04386
- Reid, M. J., Menten, K. M., Zheng, X. W., Brunthaler, A., & Xu, Y. 2009, *ApJ*, 705, 1548
- Roussel, G., Lacombe, F., Puget, P., et al. 1998, *Proc. SPIE Vol.*, 3353, 508
- Rubilar, G. F. & Eckart, A. 2001, *A&A*, 374, 95
- Sakai, S., Lu, J. R., Ghez, A., et al. 2019, *ApJ*, 873, 65
- Schmidt, M. 1963, *Nature*, 197, 1040
- Schödel, R., Gallego-Cano, E., Dong, H., et al. 2018, *A&A*, 609, A27
- Schödel, R., Merritt, D., & Eckart, A. 2009, *A&A*, 502, 91
- Schödel, R., Ott, T., Genzel, R., et al. 2002, *Nature*, 419, 694
- Schwarzschild, K. 1916, *Sitzungsberichte der Königlich Preussischen Akademie der Wissenschaften (Berlin)*, 189
- Tanaka, Y., Nandra, K., Fabian, A. C., et al. 1995, *Nature*, 375, 659
- Vincent, F. H., Paumard, T., Gourgoulhon, E., & Perrin, G. 2011, *Classical and Quantum Gravity*, 28, 225011
- Will, C. M. 2008, *ApJ*, 674, L25
- Will, C. M. 2014, *Living Reviews in Relativity*, 17, 4
- Will, C. M. & Nordtvedt, Kenneth, J. 1972, *ApJ*, 177, 757
- Yelda, S., Ghez, A. M., Lu, J. R., et al. 2014, *ApJ*, 783, 131
- Yu, Q. & Tremaine, S. 2003, *ApJ*, 599, 1129
- Zhang, F. & Iorio, L. 2017, *ApJ*, 834, 198
- Zucker, S., Alexander, T., Gillessen, S., Eisenhauer, F., & Genzel, R. 2006, *ApJ Letters*, 639, 21

Appendix A: Experimental techniques

Appendix A.1: GRAVITY data analysis

Our result crucially depends on the use of GRAVITY, the VLTI beam combiner, which as a result of its extremely high angular resolution of ≈ 3 mas yields very accurate astrometry with errors well below $100 \mu\text{as}$ (Gravity Collaboration et al. 2017 and Figure A.3). Depending on the separation between S2 and Sgr A* there are two fundamentally different ways to retrieve the separation vector between S2 and Sgr A*.

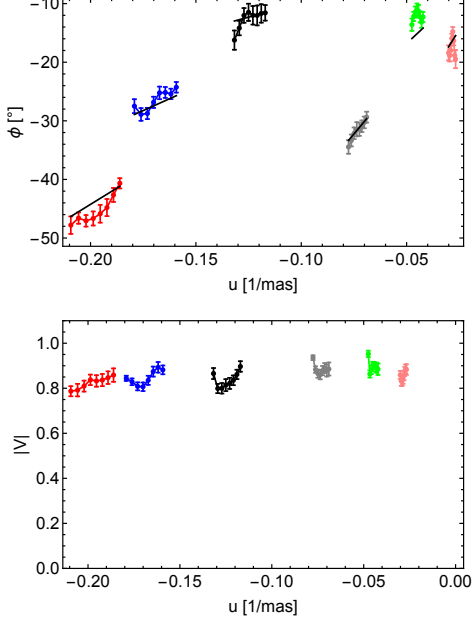


Fig. A.1. Example of a unary fit for a five-minute exposure on Sgr A* from April 22, 2019, 06:39:55. Top: Phase Φ as a function of projected baseline vector \mathbf{u} for the s-polarisation channel. Per baseline, eight spectral channels were included here. The black line is a unary model, which yields the offset from the interferometer pointing position to $\Delta\text{RA} = 322 \pm 9 \mu\text{as}$ and $\Delta\text{Dec} = 301 \pm 8 \mu\text{as}$ (formal fit errors). Bottom: The visibility modulus for the same data is constant and close to unity, consistent with the choice of fitting a single point source.

Dual-beam method. For separations larger than the single-telescope beam size (FWHM ≈ 60 mas), the GRAVITY science channel fibre needs to be pointed once to Sgr A* and once to S2, such that the respective target is the dominant source in the field. The phases of the complex visibilities of each pointing then yield an accurate distance to the fringe-tracking star, IRS16C in our case. By interferometrically calibrating the Sgr A* data with S2, the position of IRS16C drops out, and we obtain a data set in which the six phases Φ_i directly measure the desired separation vector $\mathbf{s} = (\Delta\text{RA}, \Delta\text{Dec})$ between S2 and Sgr A* through the basic interferometer formula for a unary model,

$$\Phi_{i,j} = 2\pi \mathbf{s} \cdot \mathbf{B}_i / \lambda_j, \quad (\text{A.1})$$

where \mathbf{B}_i denotes the i -th of the six baselines. Because our data are spectrally resolved into 14 channels λ_j across the K band ($2.0 \mu\text{m}$ to $2.4 \mu\text{m}$), the unknown \mathbf{s} with two parameters is well constrained by a fit to the phases. This method applies mostly to the 2019 data, and partly to the 2017 data. In Figure A.1 we show an example for such a unary fit for one Sgr A* exposure.

Single-beam method. For separations below the single-telescope beam size, both sources are observed simultaneously

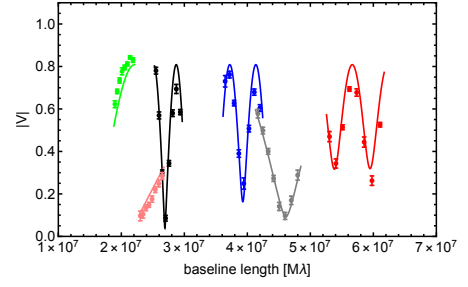


Fig. A.2. Example of a binary fit from July 8, 2017, 03:27:51. The observed visibility modulus shows strong modulation, the signature of an interferometrically resolved binary. The lines show the model for the six baselines, which includes the separation vector. The formal uncertainty in this example fit is $8 \mu\text{as}$ per coordinate.

and appear as an interferometric binary. In this case, the amplitudes of the complex visibilities as well as the closure phases carry the signature, which is a beating pattern in each baseline along the spectral axis. We fitted a binary model to these data, for which the complex visibilities are:

$$\mathbb{C}_{k,l} = \frac{I_E + \sqrt{f_k f_l} I_C}{\sqrt{I_A + f_k I_B + f_{BG} I_D} \sqrt{I_A + f_l I_B + f_{BG} I_D}}. \quad (\text{A.2})$$

In this expression we use the abbreviations

$$\begin{aligned} I_A &= I(\alpha_{\text{Sgr}}, 0), \\ I_B &= I(\alpha_{\text{S2}}, 0), \\ I_C &= I(\alpha_{\text{S2}}, \text{OPD}_{\text{S2}}), \\ I_D &= I(\alpha_{\text{BG}}, 0), \\ I_E &= I(\alpha_{\text{Sgr}}, \text{OPD}_{\text{Sgr}}), \end{aligned}$$

where

$$I(\alpha, \text{OPD}) = \int_{\Delta\lambda} P(\lambda) \lambda_{2.2}^{1-\alpha} e^{-2\pi i \text{OPD} / \lambda} d\lambda. \quad (\text{A.3})$$

The α are the spectral slopes of Sgr A*, S2, and background, and $\lambda_{2.2}$ is the wavelength λ divided by the reference wavelength $\lambda_0 = 2.2 \mu\text{m}$. The optical path differences for $X = \text{S2}$ and $X = \text{Sgr A*}$ are

$$\text{OPD}_X = \mathbf{s}_X \cdot \mathbf{B}_{k,l}. \quad (\text{A.4})$$

The function $P(\lambda)$ is the spectral bandpass, for which we used a top-hat function with a width corresponding to the measured spectral resolution. The f_k and f_l are the flux ratios of S2 to Sgr A* for telescope k and l ; f_{BG} is the flux ratio of unresolved background to the Sgr A* flux. The model yields a complex visibility for all baselines and spectral channels, of which we fit the amplitudes and closure phases to the data. We also used this analysis in our previous work (Gravity Collaboration et al. 2018a,b) and here for the 2018 and 2017 data. In Figure A.2 we show an example of how the binary model describes the visibility amplitudes for one exposure.

Appendix A.2: Details of the unary model fits

The aim is to measure the separation vector between S2 and Sgr A*. GRAVITY measures the separation between science object and fringe-tracking star (IRS16C in our case). The desired separation is obtained by measuring both S2 and Sgr A* with respect to IRS16C, and subtracting the two measurements.

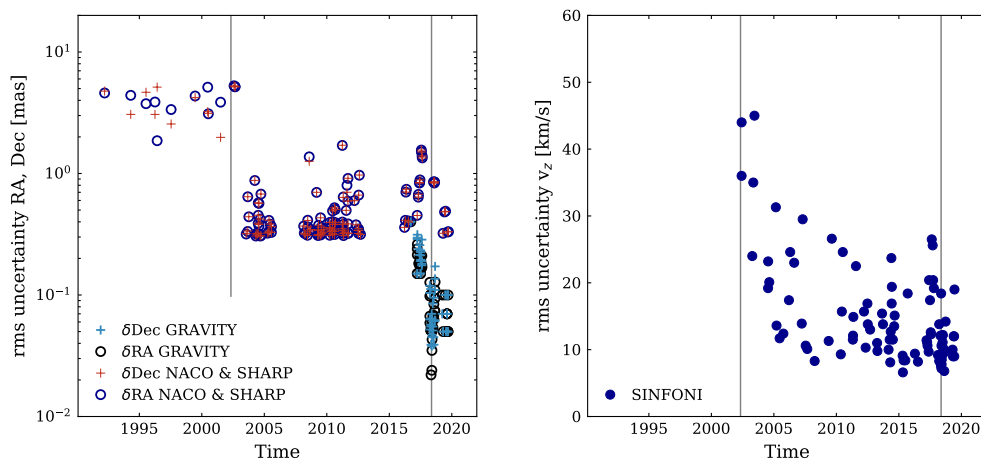


Fig. A.3. Astrometric (left) and spectroscopic (right) 1σ statistical measurement uncertainties of S2 over time. The left panel shows the almost 100-fold improvement in RA and Dec, from the early period of speckle imagery with SHARP on the 3.5 m NTT (until 2001), then the AO imagery with NACO on the 8 m VLT (>2002), and then, since 2016.7, the interferometric astrometry of GRAVITY combining all four 8 m telescopes of the VLT. The grey vertical lines are the two pericentre passages (2002.33 and 2018.38) covered by our data set.

This corresponds to interferometrically calibrating the phases of Sgr A* with those of S2.

By construction, the phases of the calibrator S2 frame are identical to 0, and ideally, the phases for all other S2 frames are 0 as well. In reality, this is not the case. At the time of observing, the separation vector \mathbf{r} between the fringe-tracking star IRS16C and S2 needs to be provided to GRAVITY for tracking the fringes with the differential delay lines. At this point, \mathbf{r} is not known to the interferometric precision, but only from the AO-data based orbital motion of IRS16C (Gillessen et al. 2017). For a subsequent S2 file, when the projected baselines have changed by some value $\Delta\mathbf{B}$ due to Earth rotation, the error in pointing $\Delta\mathbf{r}$ therefore leads to an additional phase $\Delta\Phi = \Delta\mathbf{B} \cdot \Delta\mathbf{r}$. By observing S2 a few times per night, we obtain a set of constraints for $\Delta\mathbf{r}$, which allows fitting for $\Delta\mathbf{r}$ over the course of the night.

Therefore we can correct our data post-facto for this offset $\Delta\mathbf{r}$, and obtain phases for Sgr A* that directly relate to S2. Because S2 is several interferometric beams away from Sgr A*, the phases are still wrapped, which is inconvenient for fitting. The solution is to subtract the separation vector \mathbf{r} as provided at the time of observing, and only fit (using the $\Delta\mathbf{r}$ -corrected phases) the difference to that separation.

The choice of which of the S2 frames we use as calibrator depends on the night and on the data quality of the individual files. Ideally, we seek S2 frames of good quality close in time to the Sgr A* frames, in which Sgr A* was bright. Typically, the Sgr A* frames during which the source is clearly detectable (flares of at least moderate brightness with $m_K < 16$) lead to a well-determined and stable S2-Sgr A* vector.

Appendix A.3: Details of the binary model fits

We used the binary fitting method in our previous publications (Gravity Collaboration et al. 2018a,b, 2019). The quantities used are the visibility amplitudes and the closure phases, both of which measure the internal source structure. We omit the visibility phases here, because they mostly contain information about the location of the phase centre and only to a lesser degree about the source internal structure. One of the parameters describing the source structure is the desired binary separation.

Here, we also correct for static aberrations during the binary fitting, refining our earlier procedure as a result of an improved understanding of the instrumental systematics. The aberrations are induced in the fibre coupling unit of GRAVITY and distort the incoming wavefronts depending on the source’s position in the field of view (FOV). The effect is zero at the centre of the

FOV but increases with off-axis distance and thus is of particular importance for the 2017 data where S2 and Sgr A* are detected simultaneously in a single fibre-beam positioning at a separation comparable to the fibre FOV.

We parametrise the effect of a static aberration with an amplitude A^{off} and a phase Φ^{off} on a plain wavefront in complex notation as

$$\Psi_k = E_0 A_k^{\text{off}} \exp(i\omega t + i\mathbf{s} \cdot \mathbf{x}_k + i\Phi_k^{\text{off}}), \quad (\text{A.5})$$

where k labels the telescope and \mathbf{x}_k denotes its position, E_0 is the amplitude of the unperturbed electric field, and \mathbf{s} is the source position on the sky. The scaling in amplitude A_k^{off} and the phase shift Φ_k^{off} are functions of the source position with respect to the field centre and differ for each telescope.

The GRAVITY pipeline determines the normalised interferometric visibility from the correlated flux of two telescopes divided by their respective individual fluxes. The field-dependent aberrations enter the Van Cittert-Zernike theorem as

$$V_{kl} = \frac{\int I(\boldsymbol{\sigma}) A_k^{\text{off}}(\boldsymbol{\sigma}) A_l^{\text{off}}(\boldsymbol{\sigma}) e^{\frac{2\pi i}{\lambda} \boldsymbol{\sigma} \cdot \mathbf{b}_{kl} + i\Phi_k^{\text{off}}(\boldsymbol{\sigma}) - i\Phi_l^{\text{off}}(\boldsymbol{\sigma})} d\boldsymbol{\sigma}}{\sqrt{\int I(\boldsymbol{\sigma}) (A_k^{\text{off}}(\boldsymbol{\sigma}))^2 d\boldsymbol{\sigma}} \times \sqrt{\int I(\boldsymbol{\sigma}) (A_l^{\text{off}}(\boldsymbol{\sigma}))^2 d\boldsymbol{\sigma}}}, \quad (\text{A.6})$$

where $I(\boldsymbol{\sigma})$ is the source intensity distribution and \mathbf{b}_{kl} is the projection of the baseline vector onto the plane perpendicular to the line of sight. The expression for a binary system follows from this equation and generalises Eq. A.2. The integrals in Eq. A.3 then read as

$$I(\alpha, s) = \int_{\Delta\lambda} P(\lambda) \lambda_{2.2}^{-1-\alpha} e^{-2\pi i \text{OPD}/\lambda + i\Phi^{\text{off}}(s,\lambda)} d\lambda, \quad (\text{A.7})$$

and the flux ratios f_k, f_l in Eq. A.2 are multiplied with the ratio of A^{off} for the two sources.

The refined binary fitting therefore requires maps of the amplitude and phase distortion as additional input. We obtained these from dedicated calibration runs, using the GRAVITY calibration unit, which simulates the light of an unresolved source. The offset between this source and the fibre can be controlled, and we scanned the FOV in order to measure the relative changes in phase and amplitude across (see Figure A.4 for an example).

In contrast to an astronomical observation, our calibration data are not affected by the smoothing effects of the AO residuals. We account for the atmospheric smoothing by applying a Gaussian kernel to the phase maps. The typical tip-tilt jitter for observations of the GC has an rms per-axis of ≈ 15 mas (Perrin

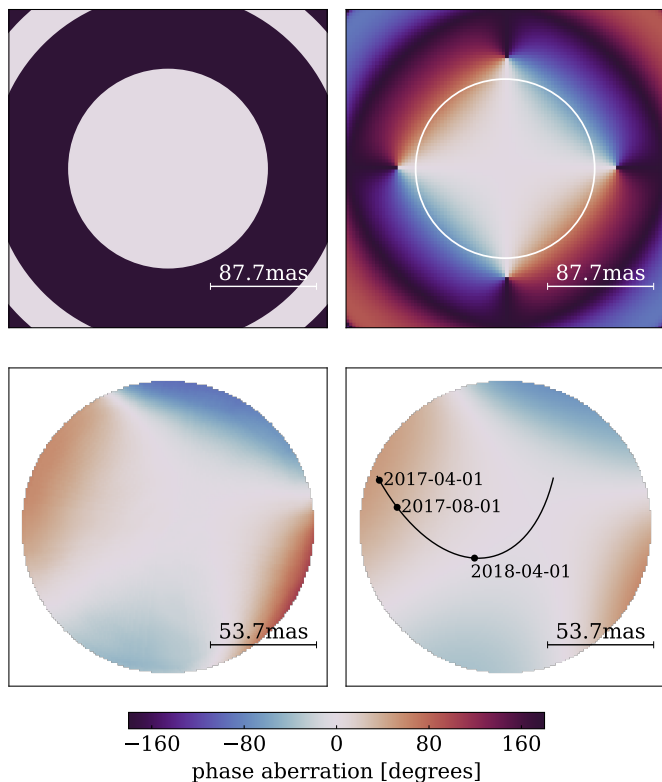


Fig. A.4. Two-dimensional phase maps used for correcting the effects of static aberrations in the binary fitting. The top row compares simulations of a perfect Airy pattern (left) to a static astigmatism with 180 nm RMS over the full pupil. The white circle in the top right panel shows the extent of the measured phase maps. One example for such a map is shown below, before (left) and after (right) applying a Gaussian kernel accounting for atmospheric smoothing. The black line in the lower right panel indicates the trace where S2 was located, as predicted by the orbit.

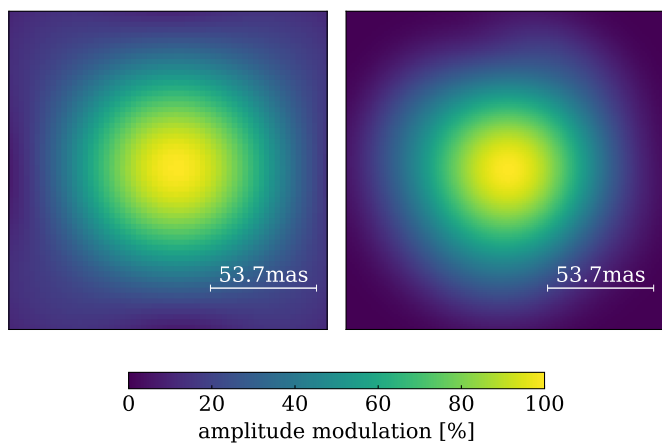


Fig. A.5. Comparison of the theoretical amplitude map smoothed with atmospheric AO residuals (left) and the measured map smoothed with a Gaussian kernel to match the on-sky measured width (right). The FWHM for the left panel is 87 mas, and for the right panel it is 88 mas.

& Woillez 2019), and higher order aberrations also contribute. We determined the amount of atmospheric smoothing by comparing the amplitude maps with the actual on-sky profiles, and verified in a simulation that the effects of a static astigmatism plus atmospheric broadening match the observed widths (Figure A.5). The uncertainty in the atmospheric smoothing yields

an additional systematic error for the astrometry that we assessed by using different smoothing kernels, which result in an FWHM of the amplitude map between 88 and 96 mas.

The effect of the static aberration does not average out, because the orientation of the field inside GRAVITY is always the same for our observations. Moreover, the projected baselines are not drawn from full tracks in the uv-plane, but we rather have a typical observing geometry. We therefore expect a bias. In comparison to binary fits neglecting static aberrations, we find that the position of S2 is indeed offset systematically throughout 2017 by approximately $0.44 \times (t - 2018) - 0.10$ mas in RA and $-0.86 \times (t - 2018) + 0.28$ mas in Dec. As expected, the offset decreases as S2 moves closer to Sgr A*. Finally, we note that our result for f_{SP} does not depend in a significant way on this correction.

Appendix B: Theoretical expectations for the precession of S2

The $12.1'$ precession angle predicted by GR corresponds to a spatial shift between the GR and the Kepler orbit of 0.78 mas at apocentre, mostly in RA because of the current orientation of the orbit. To detect this shift with 5σ significance requires a positional measurement precision of $100 \mu\text{as}$ or less. We have more than 100 NACO measurements of the orbit, each with a statistical precision of $400 \mu\text{as}$. If we did not have systematics (offset and drift of the infrared to mass-radius references frames) it should therefore (have) be(en) possible to detect the SP with NACO or the Keck NIRC imager alone. While the motion on the sky of S2 could be detected with NACO over periods of months, the GRAVITY observations detect the star's motion over 0.5 – 2 days.

The precession angle projected on the sky depends on the geometric angles of the orbit and therefore on time. In the plane of the orbit, the precession advances the angle $\delta\phi$ by $12.1'$ per orbital period of 16.046 yr. The precession projected on the sky $\delta\phi$ varies from $-17'$ to $-8.4'$ through each half SP period of $P_{SP} = 28, 710$ yr (Figure B.1).

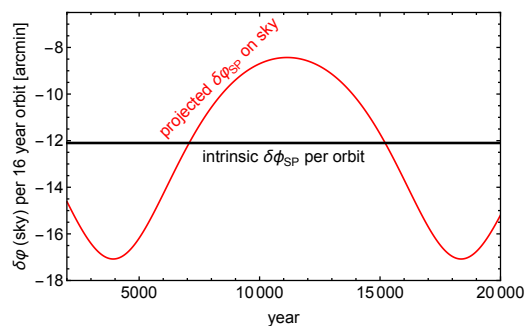


Fig. B.1. Advance of sky-projected apocentre angle $\delta\phi$, per orbital period, as a function of year.

Figure B.2 illustrates the effects the SP is expected to have on the measured parameters of the S2 orbit. Because of the strong dependence of $\delta\phi$ on radius, much of the $12.1'$ precession occurs within ± 1 year of pericentre. In RA/Dec space, the precession is seen as a ‘kink’ in the time change of the post-pericentre versus pre-pericentre residuals. Very near pericentre passage, the precession acts to first order as a time-shift between the precessing and the equivalent $f_{SP} = 0$ orbit (see also Fig. E.2 top left panel). In the residuals δRA , δDec , δv_z , and $\delta\phi$ between the data and the $f_{SP} = 0$, short-term excursions of about a few times β^2 appear in all these observables as a result.

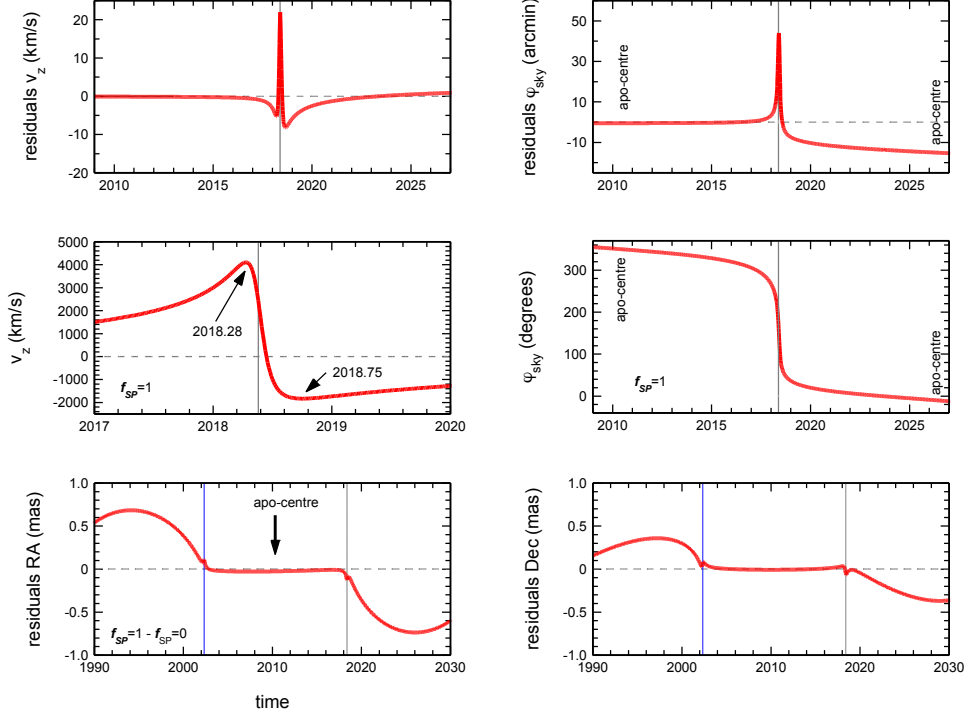


Fig. B.2. Theoretical expectations for the effect of the Schwarzschild precession on the orbit of the star S2. Here we took the best-fit parameters of the S2 orbit, and computed two model orbits, one for $f_{\text{SP}} = 0$ (Newton, plus Rømer effect, plus SRT, plus RS), and one for $f_{\text{SP}} = 1$ (equation C.1). The grey (2018.38) and blue (2002.34) vertical lines are the pericentre times. We arbitrarily set the precession angle of the SP orbit to 0 during apocentre 2010.35. The top panels denote the residuals of δv_z (left) and $\delta\varphi$ (right) between the $f_{\text{SP}} = 1$ and $f_{\text{SP}} = 0$ orbits. The bottom panels show the same for δRA and δDec (right). The middle panels present v_z (left) and φ (right) as a function of time. Here, φ is the position angle of the star on the sky, $\varphi = \arctan(\text{RA}/\text{Dec})$, running from 359° when the star is straight north, or north-west of centre, to 180° when it is straight south, to $> 0^\circ$ when it is just north-north east of centre. The most fundamental aspect of the precession is seen in the top right panel as a change in $\delta\varphi$ by $\approx 14'$ between two apocentres. Because the precession strongly depends on radius, the precession is very fast around pericentre (2018.38) in a highly elliptical orbit, so that within ≈ 1 year of pericentre $\approx 75\%$ of the precession has occurred. To first order, the precession leads to a change in time when the star is found at a given angle φ on the sky, relative to the non-precessing orbit. Because the functional form of $\varphi(t)$ is close to a step function, the differencing $\delta\varphi(t) = \varphi_{\text{SP}=1}(t) - \varphi_{\text{SP}=0}(t)$ is close to a differentiation $d\varphi/dt$, which thus results in a sharp δ -function in the residuals $\delta\varphi(t)$ near pericentre. In velocity space a similar effect occurs in the residuals as well, although $v_z(t)$ is not as symmetric in t relative to t_{peri} . Finally in δRA and δDec (bottom panels), the effect of the precession results in a ‘kink’ in the orbit coordinate time slope. Because of the variations in the foreshortening of the RA and Dec coordinates of the apocentre values of the δRA , δDec and $\delta\varphi$ the SP = 1 vs. SP = 0 curves vary over time (Figure B.1). The projected precession on the sky between the apocentres 2010.35 and 2026.5 is $\approx 14'$.

Appendix C: Parametrisation of the Schwarzschild precession

We use the post-Newtonian limit for the equation of motion presented in Will (2008), Eq. (1) therein. We parametrised the effect of the Schwarzschild metric (i.e. the prograde precession) by introducing an ad hoc factor f_{SP} in front of the terms arising from the Schwarzschild metric. We set the terms due to spin J and quadrupole moment Q_2 to 0. This results in

$$\mathbf{a} = -\frac{GM}{r^3}\mathbf{r} + f_{\text{SP}}\frac{GM}{c^2r^2}\left[\left(4\frac{GM}{r} - v^2\right)\frac{\mathbf{r}}{r} + 4i\mathbf{v}\right] + O[J] + O[Q_2]. \quad (\text{C.1})$$

In the (first-order) parameterized post-Newtonian (PPN) expansion of GR, the second term becomes

$$\frac{GM}{c^2r^2}\left[\left(2(\gamma + \beta)\frac{GM}{r} - \gamma v^2\right)\frac{\mathbf{r}}{r} + 2(1 + \gamma)i\mathbf{v}\right]. \quad (\text{C.2})$$

In GR, $\beta_{\text{GR}} = \gamma_{\text{GR}} = 1$. Two PPN parameters (β, γ) are needed to describe the equation of motion, and for no choice of β and γ can we recover the Newtonian solution. The PPN formalism is therefore less well suited for our experiment than using f_{SP} .

The net effect of the precession is

$$\Delta\phi_{\text{per orbit}} = 3f_{\text{SP}}\frac{\pi R_S}{a(1 - e^2)}, \quad (\text{C.3})$$

for our parametrisation, and to

$$\Delta\phi_{\text{per orbit}} = (2 + 2\gamma - \beta)\frac{\pi R_S}{a(1 - e^2)}, \quad (\text{C.4})$$

in the PPN formulation of GR (Will 2014). Yet it is imprecise to identify the factor $3f_{\text{SP}}$ with $(2 + 2\gamma - \beta)$. Our parameter f_{SP} characterises how relativistic the model is, as is probably easiest seen by the fact that its effect corresponds to changing the value of the speed of light in the equations, with the limit $c \rightarrow \infty$ for $f_{\text{SP}} \rightarrow 0$.

In the PPN formulation of GR, all orbits with $\beta = 2(1 + \gamma)$ have zero net precession per revolution, and all orbits with $\beta = 2\gamma - 1$ have the same amount of pericentre advance as GR. Because of the high eccentricity of the S2 orbit, the precession leads to an almost instantaneous change of the orbit orientation ω in its plane when the star passes pericentre. Our result therefore essentially compares the orbit orientations post- and pre-pericentre 2018. In this limit, we can indeed state that we have

measured $(2 + 2\gamma - \beta)/3 = 1.10 \pm 0.19$. Figure C.1 illustrates our constraint in the plane spanned by β and γ . Because there is no exact representation of the Keplerian orbit in the PPN formalism, we instead seek the PPN orbit that most closely resembles the Keplerian orbit. This depends on the eccentricity, and for S2, we find $\gamma_{\text{Kep}} = -0.78762$ and $\beta_{\text{Kep}} = 0.42476$. Changing f_{SP} corresponds to moving along a line from $(\gamma_{\text{Kep}}, \beta_{\text{Kep}})$ to $(\gamma_{\text{GR}}, \beta_{\text{GR}})$. With this, we find $\beta = 1.05 \pm 0.11$ and $\gamma = 1.18 \pm 0.34$, and the two are fully correlated.

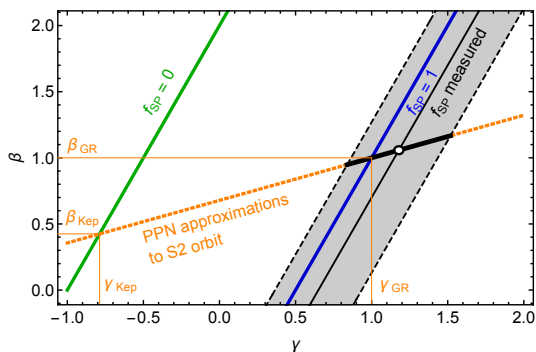


Fig. C.1. Interpretation of our measurement in the plane of the PPN parameters β and γ . Our value for f_{SP} and its uncertainty are represented by the black line and grey band. The GR value $f_{\text{SP}} = 1$ is the blue line, and the Newtonian value $f_{\text{SP}} = 0$ is the green line. The best approximations to the orbits by PPN parameters are shown by the orange dotted line. Assuming GR is a PPN theory, our measurement corresponds to the white circle at the intersection point and the uncertainties are the adjacent black thick lines.

Appendix D: Astrophysical implications

Distributed mass component inside the orbit of S2: An extended mass component would create retrograde Newtonian precession. Our data strongly constrain such a component. For simplicity we use spherically symmetric distributions of the extended mass. Using a Plummer (1911) profile with a scale parameter of 0.3 arcseconds (Mouawad et al. 2005) and fitting for the normalisation of that mass component assuming $f_{\text{SP}} = 1$ shows that $(0.00 \pm 0.10)\%$ of the central mass could be in such an extended configuration. Changing the radius parameter to 0.2 or 0.4 arcseconds yields $(-0.02 \pm 0.09)\%$ or $(0.01 \pm 0.11)\%$. Using instead a power-law profile with logarithmic slope between -1.4 and -2 results in a mass estimate of $(-0.03 \pm 0.07)\%$. Overall, we estimate that for typical density profiles the extended mass component cannot exceed 0.1%, or $\approx 4000M_{\odot}$ (1σ limits). For comparison, modelling of the star cluster suggests that the total stellar content within the apocentre of S2 is $< 1000M_{\odot}$, and the mass of stellar black holes within that radius is $80 - 340M_{\odot}$ (Figure D.1, cf. Genzel et al. 2010; Alexander 2017; Baumgardt et al. 2018). We conclude that the expected stellar content within the S2 orbit is too small to significantly affect the SP.

Merritt et al. (2010) investigated for which configurations the Newtonian precession due to an extended mass component in the form of individual stellar mass objects exceeds the effects of spin and quadrupole moment of the MBH. They addressed a range of masses between 1 and $10^3 M_{\odot}$ in the central milliparsec. The above limits translate into a limit of $\approx 200 M_{\odot}$ in that radial range. Figure 1 of Merritt et al. (2010) shows that for S2 itself, our limit on the extended mass would lead to perturbations almost on par with the expected spin effects for a maximally spinning MBH, giving some hope that the spin of Sgr A*

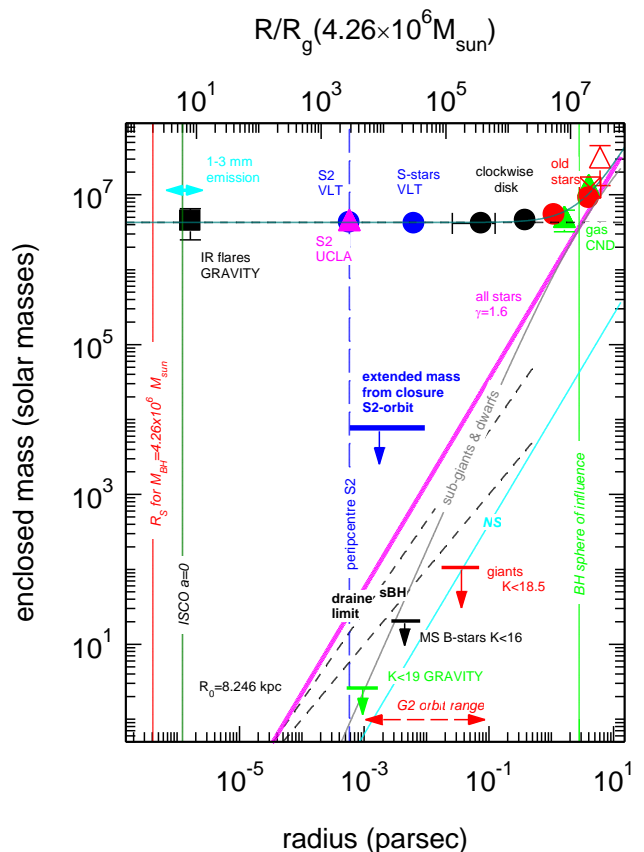


Fig. D.1. Constraints on the enclosed mass in the central 10 pc of the Galaxy. The blue crossed circle, the pink triangle, and the black crossed rectangles are estimates of the enclosed mass within the S2 orbit, other S-stars and the massive star discs (Paumard et al. 2006; Bartko et al. 2009; Yelda et al. 2014). The red filled circles, the red crossed rectangle, and red open triangles denote mass measurements from late-type stars. Green triangles are mass estimates from rotating gas in the circum-nuclear disc (see Genzel et al. 2010 for details). The filled black rectangle comes from the clockwise loop-motions of synchrotron near-infrared flares (Gravity Collaboration et al. 2018b). The cyan double arrow denotes current VLBI estimates of the 3 mm size of Sgr A* (Issaoun et al. 2019). The continuous magenta line shows the total mass from all stars and stellar remnants (Alexander 2017). The grey line marks the distribution of $K < 18.5$ sub-giants and dwarfs from Schödel et al. (2018). The black dashed lines and the cyan line indicate the distribution of stellar black holes and neutron stars from theoretical simulations of Alexander (2017) and Baumgardt et al. (2018), which span a range of roughly a factor 5. Red, black and green upper limits denote upper limits on giants, main-sequence B stars and $K < 19$ GRAVITY sources. The Schwarzschild radius of a $4.26 \times 10^6 M_{\odot}$ black hole and the innermost stable circular orbit radius for a non-spinning black hole are given by red vertical lines. The pericentre radius of S2 is the dashed vertical blue line and the sphere of influence of the black hole is given by the vertical green line. The blue horizontal line denotes the 2σ upper limit of any extended mass around Sgr A* obtained from the lack of retrograde precession in the S2 orbit (see text).

can eventually be detected from S2 despite its large orbital radius. Zhang & Iorio (2017) cautioned, however, that already the Newtonian perturbation from S55/S0-102 (Meyer et al. 2012; Gillessen et al. 2017) might hide the spin's signature. For stars on shorter period orbits or with higher eccentricities, detecting the higher order effects of the metric is easier; and stellar perturbations have a different observational signature than the effect of the metric.

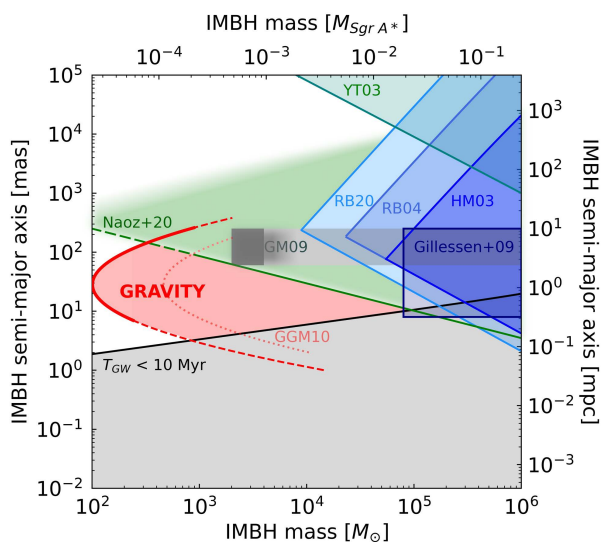


Fig. D.2. Limits on a second, intermediate mass black hole (IMBH), as a function of its mass and separation from Sgr A*. The shaded area is excluded observationally. Adapted from Gualandris & Merritt (2009). The blue shaded regions are due to the lack of observed motion of Sgr A* at radio wavelengths (Hansen & Milosavljević 2003, HM03). The data from Reid & Brunthaler (2004, RB04) and Reid & Brunthaler (2020, RB20) improve these limits. The upper bound results from the limit on the 3D velocity $v_{3D} \lesssim 8$ km/s (RB04) and $\lesssim 3$ km/s (RB20). The lower bound results from the absence of short-period fluctuations in the position, with limits of 1 mas and 0.5 mas in RB04 and RB20. Yu & Tremaine (2003) set a limit from the ejection rates of hypervelocity stars if an IMBH were present in the GC (YT03). The bottom area is excluded because the gravitational wave inspiral time scale T_{GW} would be < 10 Myr. Naoz et al. (2020) exclude the green shaded area by demanding that the S2 orbit be stable, taking into account resonant effects from the IMBH. Beyond the ranges given in the original work, the constraints get weaker (fading color). The area labeled GM09 is excluded by Gualandris & Merritt (2009), who calculated the effect of an IMBH on the distribution of stellar orbits. Their original box extends to higher masses (shaded area to right). A first constraint from the orbit data of S2 was given in Gillessen et al. (2009b). Extending the orbital coverage in a simulation to the 2018 pericentre passage Gualandris et al. (2010) concluded that from a lack of extra residuals one should be able to exclude the area right of the dotted line (GGM10). GRAVITY improved the accuracy compared to these simulations by a factor 4.6, which moves the limit further to lower masses (red-shaded region). All but a $10^2 - 10^3 M_{\odot}$ IMBH inside or just outside of S2’s orbit is now excluded by the various measurements. This also excludes the configurations Merritt et al. (2009) found to be efficient in randomizing the S-star orbits.

A second massive object in the GC: The presence of an intermediate mass black hole (IMBH) orbiting Sgr A* inside the orbit of S2 is constrained by our measurements. Gualandris et al. (2010) explored a grid of three-body simulations with an IMBH of mass 400 to $4000 M_{\odot}$ on orbits similar in size to the S2 with a range of angles and eccentricities relative to the S2 orbit. By inspecting the astrometric and spectroscopic residuals from the three-body system in comparison to the assumed astrometric error, they concluded that the 2018 pericentre passage of S2 would exclude a large part of the parameter space. The additional data since 2010 and the much more accurate astrometry from GRAVITY now exclude any IMBH greater than about $1000 M_{\odot}$ in the central arcsecond, and allow IMBHs in the mass range of $100 - 1000 M_{\odot}$ only in a small region inside or just outside of the orbit of S2 (Figure D.2). In the radial regime of the stellar discs ($1'' - 10''$) an IMBH of up to $10^4 M_{\odot}$ is still allowed.

The distance to the GC: Our data set continues to constrain R_0 ever better. Setting $f_{SP} = f_{RS} = 1$ fixed during the fit, we obtain our best estimate for $R_0 = 8248.6 \pm 8.8$ pc, where the error is the statistical error alone. This is 25% more precise than our result in Gravity Collaboration et al. (2019), but the values differ by $\approx 2\sigma$ when we take the systematic error from Gravity Collaboration et al. (2019) into account. We now conservatively adopt, with the improved data set, a systematic error of 45 pc, which is twice as large as before. This better reflects the variations between Gravity Collaboration et al. (2018a), Gravity Collaboration et al. (2019) and this work. Our current best estimate is therefore $R_0 = 8249 \pm 9|_{\text{stat.}} \pm 45|_{\text{sys.}}$ pc. Because of the strong correlation between the best-fit MBH mass M_{\bullet} and R_0 (Figure E.2), the increase in R_0 is reflected in M_{\bullet} .

Constraints on PPN parameters: In Appendix C we derived our constraints on the PPN parameters $\beta = 1.05 \pm 0.11$ and $\gamma = 1.18 \pm 0.34$. These are consistent with GR, but not competitive with the results obtained in the Solar System from spacecraft measurements. The deviation from the GR value of $\gamma = 1$ is best constrained through the Shapiro delay from the Cassini spacecraft to better than 2×10^{-5} , while VLBI measurements of the light deflection using the quasars 3C273 and 3C279 yield a factor 10 weaker constraints on γ (Will 2014). Assuming the value of γ from Cassini, the SP of Mercury’s orbit from the Messenger spacecraft yields a constraint on β of 8×10^{-5} . While our constraints are weaker, they probe a completely different regime in mass (by a factor 4×10^6) and potential strength (by a factor 10^2 to 10^4) than the Solar System tests (Figure D.3).

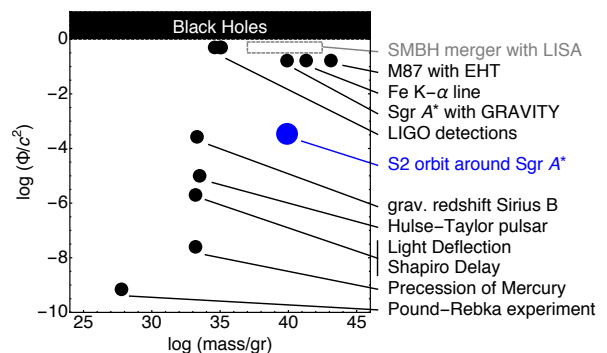


Fig. D.3. Comparison of tests of GR in the plane of mass and potential, adapted from Psaltis (2004). Black: Terrestrial laboratories, Mercury’s precession, light deflection, and Shapiro delay in the Solar System, the Hulse-Taylor pulsar, the LIGO detections, the relativistic K- α lines, and the M87 EHT observation. LISA signals will probe the grey rectangular region. This work, using S2, is marked in blue.

Beyond the standard model: We also derived limits on a Yukawa-like potential in the GC (Hees et al. 2017). Our limits show the same sensitivity to the length-scale parameter λ as in Hees et al. (2017), but are a factor 20 more constraining in terms of the interaction strength α . At our most sensitive $\lambda = 180$ AU, we constrain $|\alpha| < 8.8 \times 10^{-4}$ (95% confidence level).

Our data also constrain the possible parameters for an assumed dark-matter spike in the GC. Lacroix (2018) showed that for a Navarro-Frenk-White profile (Navarro et al. 1996) with slope $\gamma = -1$ plus a spike with a power-law profile with slope $\gamma_{sp} = -7/3$, the data of Gillessen et al. (2017) constrain the spike radius to $R_{sp} \lesssim 100$ pc, corresponding to an enclosed mass of $\approx 5 \times 10^4 M_{\odot}$. Our new data set constrains $R_{sp} \lesssim 10$ pc (corresponding to $\approx 3 \times 10^3 M_{\odot}$), which is just below the theoretical prediction from Gondolo & Silk (1999), who took limits from the absence of a neutrino signal from the GC into account.

Table E.1. Best-fit orbit parameters. The orbital parameters are to be interpreted as the osculating orbital parameters. The argument of periapsis ω and the time of pericentre passage t_{peri} are given for the epoch of last apocentre in 2010.

Parameter	Value	fit error	MCMC error	Unit
f_{SP}	1.10	0.19	0.21	
f_{RS}	1	fixed	fixed	
M_{\bullet}	4.261	0.012	0.012	$10^6 M_{\odot}$
R_0	8246.7	9.3	9.3	pc
a	125.058	0.041	0.044	mas
e	0.884649	0.000066	0.000079	
i	134.567	0.033	0.033	$^{\circ}$
ω	66.263	0.031	0.030	$^{\circ}$
Ω	228.171	0.031	0.031	$^{\circ}$
P	16.0455	0.0013	0.0013	yr
t_{peri}	2018.37900	0.00016	0.00017	yr
x_0	-0.90	0.14	0.15	mas
y_0	0.07	0.12	0.11	mas
v_{x0}	0.080	0.010	0.010	mas/yr
v_{y0}	0.0341	0.0096	0.0096	mas/yr
v_{z0}	-1.6	1.4	1.4	km/s

Appendix E: Details of the fit

In Table E.1 we report the best-fitting parameters of our 14-parameter fit, together with the formal fit errors and the 1σ confidence intervals from the MCMC. The two approaches agree because our fit is well behaved. There is a single minimum for χ^2 , and the posterior distribution is close to a 14-dimensional Gaussian (Figure E.3), with significant correlations, however. Figure E.1 shows the posterior for f_{SP} .

In Figure E.2 we show selected correlation plots from the posterior distribution, which are worth discussing in the context of f_{SP} . The strongest correlation for f_{SP} is with the pericentre time. This is not surprising, given the discussion in Appendix B, where we showed that near pericentre the SP acts like a shift in time. The second strongest correlation for f_{SP} is with the RA offset of the coordinate system. This explains why including the NACO flare data helps determining f_{SP} : The flares essentially measure the offset of the coordinate system.

The parameter f_{SP} is also weakly correlated with the semi-major axis a and it is anti-correlated with the eccentricity e of the orbit. The former can be understood in the following way: If the orbit were slightly larger on sky, a stronger precession term would be required in order to achieve the same amount of kink (in mas on sky) at pericentre. The latter is understood similarly: A higher eccentricity leads to a narrower orbit figure, and hence less of the precession term would be needed. Interestingly, f_{SP} is almost uncorrelated with the argument of periapsis ω (i.e. the angle describing the orientation of the orbital ellipse in its plane), despite that the SP changes exactly that parameter.

The strongest correlation between any two parameters for our fit is the well known degeneracy between mass M_{\bullet} and distance R_0 (Ghez et al. 2008; Gillessen et al. 2009b; Boehle et al. 2016; Gillessen et al. 2017; Gravity Collaboration et al. 2018a, 2019). The parameter f_{SP} is only very weakly correlated with R_0 .²

² **Note added in proof:** After acceptance of this paper we noticed posting Gainutdinov (2020). He uses a subset of the data presented here for S2 (measurements taken until 2018), as well as published measurements for the stars S38 and S102, to put constraints on the PPN parameters β and γ . He finds an approximately two-sigma agreement with the value

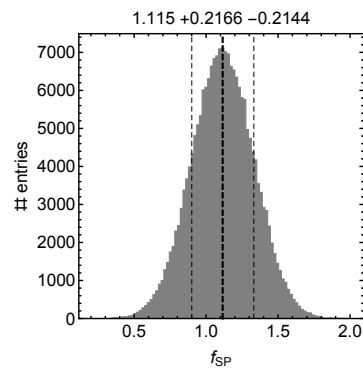


Fig. E.1. Result of the MCMC modelling of our data, showing the posterior distribution of the Schwarzschild parameter f_{SP} .

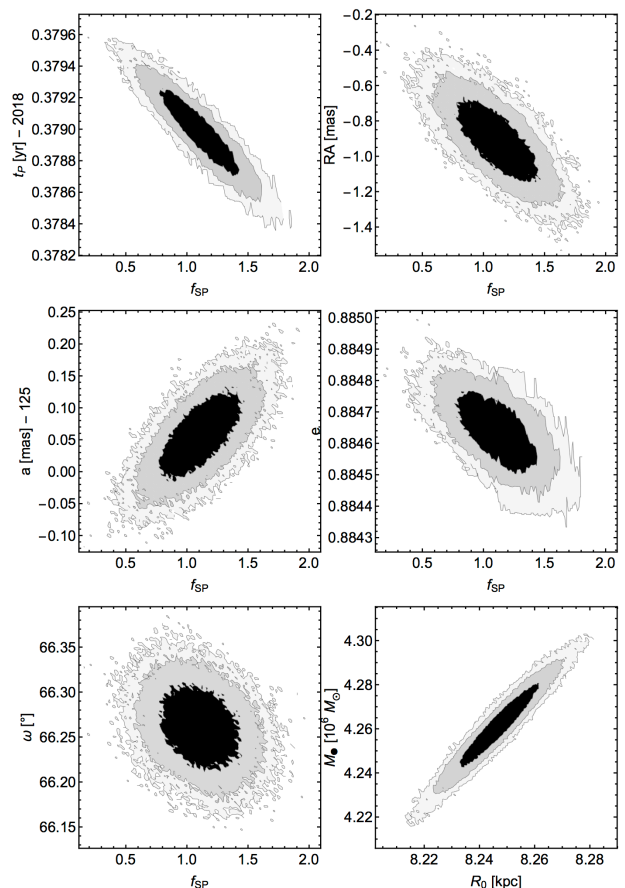


Fig. E.2. Selected parameter correlations from the 14-dimensional posterior distribution as determined from MCMC modelling.

of unity expected in GR. His analysis however fixes the values of the black hole mass and distance, v_{x0} , v_{y0} and v_{z0} as well as x_0 and y_0 in advance, which naturally leads to significantly underestimated error bars. Further, the analysis combines data sets from the VLT and Keck telescopes, without allowing for a coordinate system offset, which however is known to be essential (Gillessen et al. 2009a).

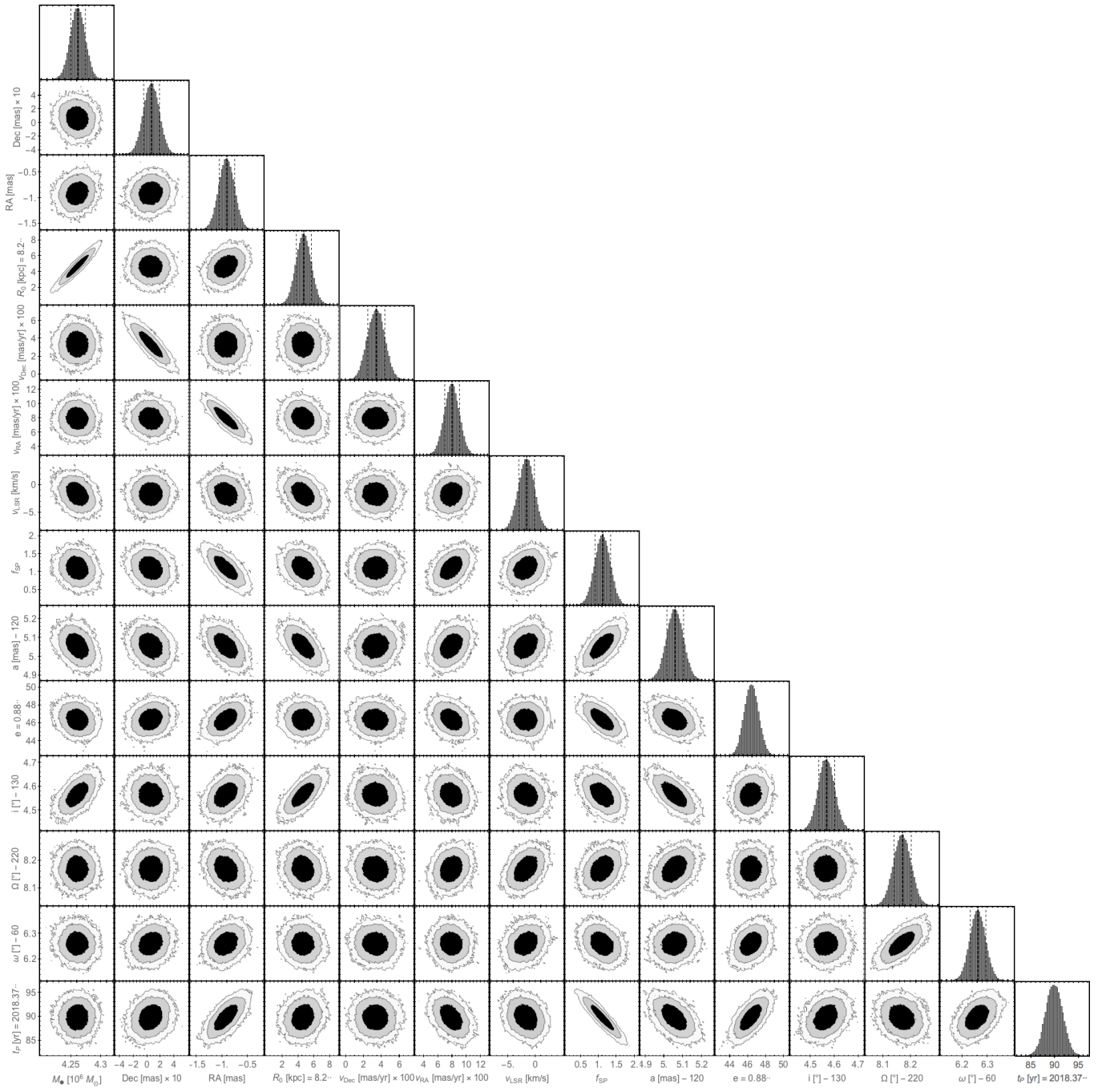


Fig. E.3. Full, 14-dimensional posterior distribution of our orbit fit.